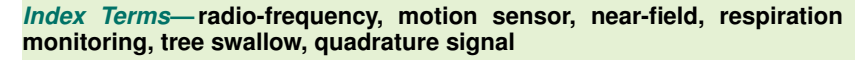
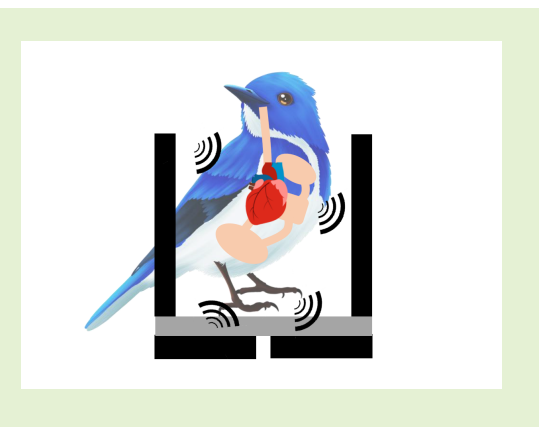


Radio-Frequency Near-Field Sensor Design for Minuscule Internal Motion

Jianlin Zhou, Student Member, IEEE, Conor C. Taff, David A. Chang van Oordt, Maren N. Vitousek, and Edwin C. Kan, Senior Member, IEEE

Abstract—We present the improved design of a radio-frequency (RF) near-field sensor for minuscule internal motion inside structures and small animals. The design tradeoffs of the antenna placement and transceiver configuration are explored experimentally by a structural setup of the fluid stirrer. The sensor performance is benchmarked in various antenna configurations and quadrature baseband sampling settings. An optimized antenna pair holder design is then applied to a continuous touchless recording for the respiration and heartbeat of nestling and adult tree swallows non-invasively. Furthermore, we also built a low-power portable all-in-one RF sensor PCB using the system parameters from previous experiments. A 40-minute experiment on a conscious and free-to-move 13-day old nestling tree swallow for respiration monitoring was successfully conducted.





I. INTRODUCTION

ONINVASIVE or covert monitoring of minuscule internal motion hidden inside a mechanical structure or a small conscious animal is difficult for present sensors by imaging or ultrasound due to the requirement of temporal and spatial resolution as well as possible surface preparation requirements. However, many scientific and engineering applications would benefit greatly from this new sensing ability. For example, monitoring small animal vital signs is critical for analyzing its metabolism and biological reaction to environmental changes and stimuli [1], [2]. In addition, the vibration of steel bars inside concrete load beams behind dry walls can serve as structural integrity indicators during periodic maintenance schedule [3]. In comparison, accelerometer and gyroscopebased motion sensing methods are well established and have been applied to structural vibration monitoring and human vital-signs monitoring [4], [5]. Accelerometer and gyroscopebased motion sensors have small size and low power consumption which enable their integration to a wearable or long term motion sensing system. However, these techniques require

This project is supported by US Army Discovery Award through the CDMRP Program PR182496 and by US Department of Energy ARPA-E Project DE-AR0000946 and National Science Foundation grant NSF-IOS 2128337.

The animal experiments are under Cornell IACUC Protocol 2019-0023.

- J. Zhou and E. C. Kan are with the School of Electrical and Computer Engineering, Cornell University, Ithaca, NY 14853, USA. E-mails: {jz899; eck5}@cornell.edu.
- C. C. Taff, D. A. Chang van Oordt and M. N. Vitousek are with the Lab of Ornithology and Department of Ecology & Evolutionary Biology, Cornell University, Ithaca, NY 14853, USA. E-mails: {cct63; dac385; mnv6}@cornell.edu.

direct contact with the sensing subject and can have degraded signal quality when internal motion cannot be effectively transduced to the surface due to the structural property, existing air layers or bubbles, and mounting conditions [6].

While offering fully non-contact operation and detectability of minute surface motion, far-field microwave sensors often require a direct line-of-sight (LoS) with the subject's moving surface or additional tags attaching to the surface [7]–[13]. Poor energy coupling to the internal motion source due to large surface reflection can also degrade the sensing performance significantly. Near-field radio-frequency (RF) sensing can provide solutions to some of the limitations of far-field sensors [14], [15]. Wearable devices allow subjects to move freely during monitoring and couple electromagnetic energy efficiently into the hidden internal motion source in the local near-field zone, whereas far-field sensing often detects mainly surface motion [16]-[18]. Thus, for sensing subjects whose internal motion does not render surface vibration or monitoring the vital signs of small animals with least surface preparation and invasiveness, the near-field method can be advantageous [19]–[21].

In this work, we present the improved design of a near-field RF sensor for minuscule internal motion inside mechanical structures and small animals. The benchmark system of the near-field RF sensing by a fluidic stirrer model is described in Section II. In Section III, we experimentally analyzed the sensing performance of different antenna placements and quadrature sampling configurations. As the motion ground truth for the mechanical model is known, we were able to benchmark the feasible system parameters, which were then applied to the illustrative experiments on respiration

and heartbeat monitoring of both nestling and adult tree swallows (Tachycineta bicolor) in Section IV. In Section V, for comprehensive analysis of the bird metabolism, we used the system parameters from previous experiments to build a low-power portable all-in-one RF sensor, which is integrated into an air-tight chamber with the sensing of temperature, O_2/CO_2 concentrations, and motion levels.

II. SYSTEM ARCHITECTURE AND STIRRER MODEL A. Near-Field RF Sensor

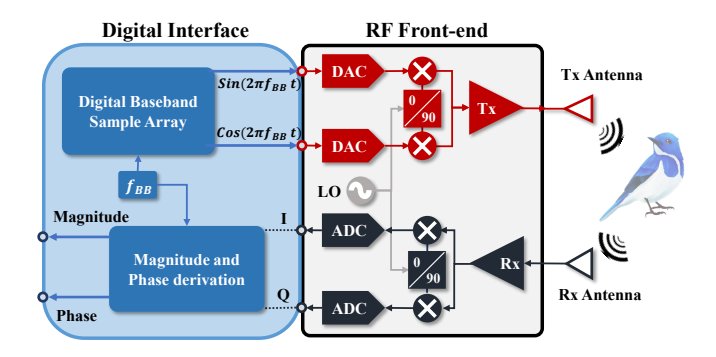


Fig. 1. The block diagram of the near-field RF transceiver.

The block diagram of the RF near-field transceiver is shown in Fig. 1, which includes two main modules. The RF frontend is implemented by a Universal Software Radio Peripheral (USRP) on a software-defined radio (SDR) platform (National Instrument Ettus Research B200). We employed the quadrature scheme on the digital baseband tone f_{BB} , which was fed into the digital-to-analog converter (DAC) and then mixed with the local oscillator (LO) frequency f_{LO} . The RF emitting power was less than $0.1 \, mW$, which was below the safety limits set by occupational safety and health administration (OSHA) in the ultrahigh frequency (UHF) band [22]. The transmitter (Tx) signal was coupled into the sensing target, modulated by the nearby dielectric motion, received by the receiver (Rx), and then down-converted and sampled by the analog-to-digital converter (ADC) to retrieve the in-phase (I) and quadrature (Q) baseband signals. Due to the high ADC sampling rate for SDR built for communication purposes, it is often unnecessary to save the raw I/Q samples for sensing output. Therefore, the magnitude and phase of our complex quadrature baseband signal are derived and saved only after downsampling.

B. Stirrer Model

In order to analyze how antenna placement and baseband radio configuration affect sensor performance on minuscule internal motion, we constructed a model which can simulate simple internal structural motion in a repeatable and consistent manner. Furthermore, the dielectric properties of the moving target, its background material, and the outer structure layers and shapes can give different results. We proposed a motion simulator design in which internal motion amplitude and structure material properties are adjustable, as shown in Fig. 2. A magnetic stirrer structure (INTLAB MS-500) was used

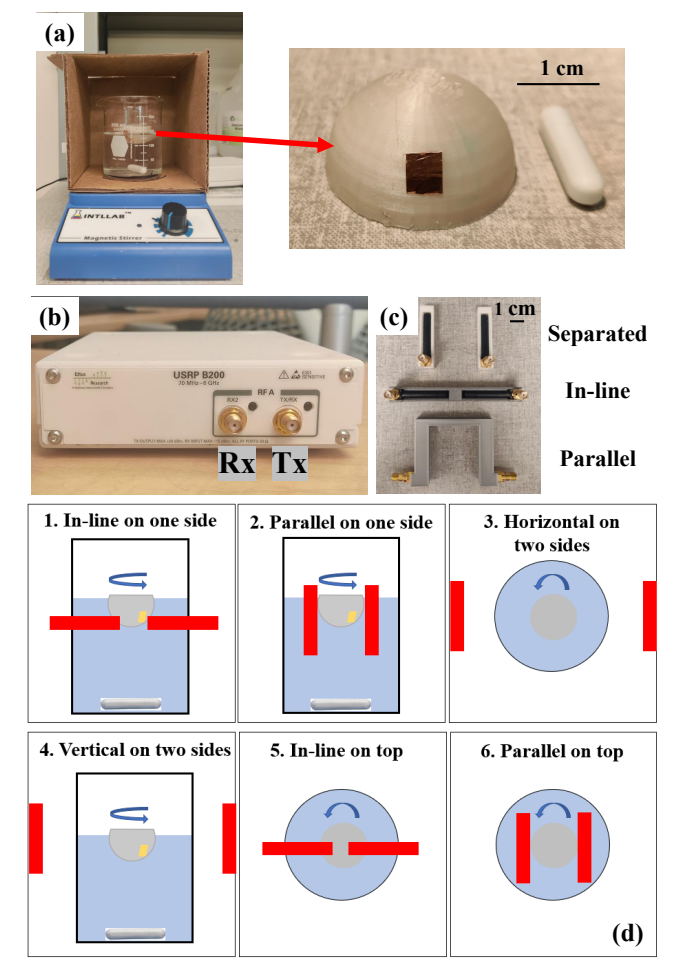


Fig. 2. (a) The stirrer model and the semilunar shell float. (b) USRP B200. (c) Three antenna pair holders for in-line, parallel and separated placements. (d) Different antenna pair placements for internal motion sensing.

to rotate the magnet bar inside a small beaker which is filled with 150 mL of water. The amplitude and speed of the motion source can be adjusted by the infilling liquid volume and viscosity properties. A 6 mm × 6 mm copper strip was mounted on the surface and at the 10 mm level from the bottom of a 3D-printed semilunar shell (Polylactic acid), which has a thickness of 2 mm and a radius of 20 mm. Motion speed and amplitude can be further modified accordingly by changing the size, material, and placement of the semilunar shell and the reflector. The stirrer rotated the semilunar shell through water as the internal motion source. As shown in Fig. 2(c), three different types of whip antenna (Taoglas TG.22.0112) pair holders (in-line, parallel, and separated) were tested. The distance of the Tx and Rx antennas was 50 mm from the physical center when they were placed in-line and parallel. In human vital-sign applications, the antenna pair was either in-line or parallelly placed on one side of the body due to deployment convenience. However, for small structures or animals, it is also possible to deploy the Tx antenna and Rx antenna on the two sides in a multi-static manner. Hence, we evaluated six antenna placements with the three antenna holder structures on the side or on the top of a cardboard frame, as shown in Fig. 2(d).

III. NEAR-FIELD RF SENSING SIGNAL AND DESIGN CONSIDERATION

A. Quadrature Signal Processing

In the RF near-field sensing, the Rx signal consisted of both the signal modulated by the target dielectric boundary motion and the direct-path signal from Tx to Rx without modulation. After downconversion, the carrier frequency component (f_{LO}) would be removed. The Rx signal was further sampled as the baseband quadrature signals as the I and Q parts, which were given by:

$$I_{RX}(t) = S_{RX}(t)\cos(2\pi f_{BB} + \theta_{RX}(t) + \theta_o) \qquad (1)$$

$$Q_{RX}(t) = S_{RX}(t)\sin(2\pi f_{BB} + \theta_{RX}(t) + \theta_o) \qquad (2)$$

where $S_{RX}(t)$ and $\theta_{RX}(t)$ are the Rx quadrature complex signal magnitude and phase. In practice, due to the random initial phase of the local oscillator (LO) synthesizer, and antenna detuning caused by ambient variation, a random phase offset θ_o also needs to be added. Traditionally, the near-field radio sensing signals were processed by the signal magnitude MAG_{RX} and phase PH_{RX} separately, which can be retrieved from:

$$MAG_{RX}(t) = \sqrt{I_{RX}(t)^2 + Q_{RX}(t)^2}$$
 (3)

$$PH_{RX}(t) = unwrap(tan^{-1}\frac{Q_{RX}(t)}{I_{RX}(t)} - 2\pi f_{BB}t) \quad (4)$$

Here, we can find that the sampled I, and Q waveforms can also be represented by a complex phasor from the recorded magnitude and phase samples:

$$\overrightarrow{V}[n] = MAG_{RX}[n] \angle PH_{RX}[n] \tag{5}$$

where n is the index for the time stamp after sampling. And the complex phasor can be further expressed as:

$$MAG_{RX}[n] \angle PH_{RX}[n] = S_{RX}[n] \angle (\theta_{RX}[n] + \theta_o)$$
 (6)

In our previous work [23], we demonstrated that the random phase offset θ_o can significantly change the magnitude and phase waveform morphology, which was also shown in Figs. 3(c) and 3(d). This common-mode random phase offset complicated the comparison of signal characteristics caused by antenna placement and radio configuration quantitatively and consistently. To reduce the impact of θ_o , a phase regularization processing was performed on the complex phasor signals. In order to mitigate the random phase θ_o , we first translated the complex vector signal to the center of origin:

$$\overrightarrow{V_{center}}[n] = \overrightarrow{V}[n] - (\overline{(real(\overrightarrow{V}[n]))} + j\overline{(imag(\overrightarrow{V}[n]))}) \quad (7)$$

where $(real(\overrightarrow{V}[n]))$ and $(imag(\overrightarrow{V}[n]))$ were the mean values of the signals' real and imaginary part. And θ_o can be calculates from:

$$\theta_o = tan^{-1}(pinv(real(\overrightarrow{V_{center}}[n])) \times imag(\overrightarrow{V_{center}}[n]))$$
(8

where pinv was the MATLAB Moore-Penrose pseudo-inverse function. Once θ_o was calculated, all the complex samples are multiplied by a phasor $e^{j(\pi/4-\theta_o)}$. As shown in Figs. 3(a) and 3(b), complex samples were normalized to the same commonmode angle, which can help us align the sample distribution along the same direction and regularize the magnitude and phase morphology of the complex signal [23].

B. Sensor Design Consideration

TABLE I
DIFFERENT ANTENNA PLACEMENTS AND CORRESPONDING SIGNAL
FEATURE COMPARISON.

	Magnitude SNR (dB)		Phase SNR (dB)	
	Fund.	2 nd	Fund.	2 nd
		narmonic		narmonic
1.In-line; side	18.6	2.3	6.0	13.6
2.Parallel; side	17.1	17.9	20.8	11.3
3.Horizontal; 2 sides	17.4	7.9	13.8	6.8
4. Vertical; 2 sides	8.9	14.6	9.8	14.6
5.In-line; top	21.7	9.2	12.0	13.8
6.Parallel; top	6.0	13.8	7.7	6.8

In the stirrer model, a pair of monopole helical whip antennas (Taoglas TG.22.0112) packed in a 3D-printed fixture was connected to the Tx and Rx of the SDR. The carrier frequency was set to 900 MHz with f_{BB} = 50 kHz. I and Q signals were sampled at 10⁶ sample per second (Sps), and then the calculated magnitude and phase waveforms were downsampled to 5×10^5 Sps after an anti-aliasing filter. We first reconstructed and centered the complex signal and regularized the phase offset to $\pi/4$ before further analyses of the magnitude and phase waveforms. We tested six different antenna pair placements as shown in Fig. 2(c), and their timedomain magnitude and phase signals, as well as the corresponding spectra, are shown in Fig. 4(a) and (b). We can find the signal from in-line placement on one side has the largest magnitude, and the signal from parallel placement on the top shows the least magnitude. We also calculate the fundamental tone and 2^{nd} harmonic signal-to-noise ratio (SNR), which are determined by the maximum peaks between 3 Hz to 4 Hz and 6 Hz to 8 Hz from the power spectrum to the average reading between 1 Hz to 10 Hz, as shown in Table.I. We can find that in-line placement provides the largest fundamental-tone SNR. Two parallel placements and the vertical placement on two sides all have a stronger harmonic than the fundamental tone. We believe this is because of the structural symmetry and cyclic motion. Thus, in-line placement is preferred for applications where the fundamental rhythm is more important. If higher-order harmonics of the fundamental tone signal are needed, parallel placements can be better.

Furthermore, we also investigated the impact of f_{BB} and the I/Q sampling rate. A 4000-sample buffer is used to generate the digital baseband signal. We first tried f_{BB} = 400 Hz and 1000 Hz with I/Q sample rates ranging from 2000 Sps to 4000

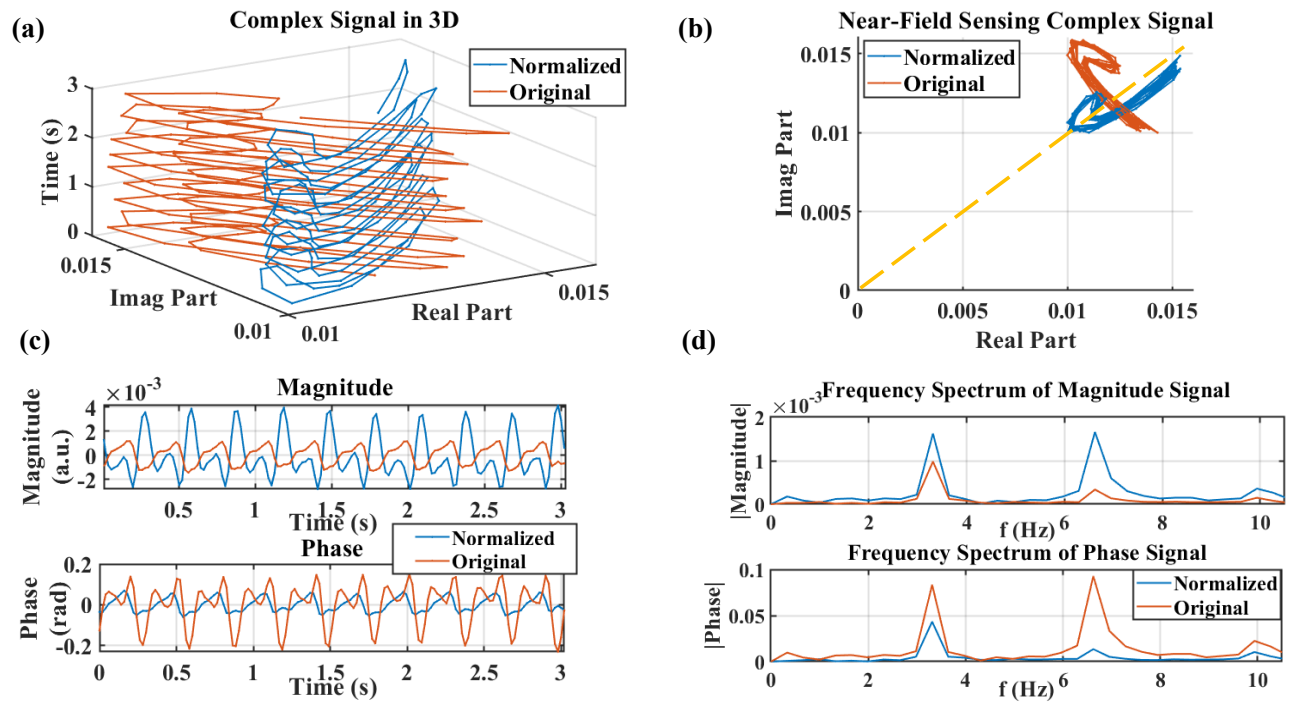


Fig. 3. An example of the complex quadrature signal representations of semilunar shell float motion before and after phase regularization, and the corresponding magnitude and phase waveform morphology. (a) The original and regularized near-field signal in time-complex domain representation. (b) The phase regularization only rotates the complex signal without changing its features. In the time-domain (c) and in the frequency domain (d), by removing θ_0 and assigning a fixed phase $\pi/4$, the signal magnitude and phase characteristics can change significantly.

TABLE II SNR OF THE FUNDAMENTAL TONE AND 2^{nd} HARMONICS FOR VARIOUS f_{BB} AND SAMPLING-RATE CONFIGURATIONS.

I/Q sample rate (Hz)	f_{BB} (Hz)	Magnitude SNR fund. tone (dB)	Magnitude SNR 2^{nd} harmonic (dB)
8k	1.6k	-1.3	-9.9
8k	2k	2.4	0.4
6k	2k	2.4	-0.2
100k	2k	15.7	7.8
100k	8k	14.2	9.0
100k	9k	14.6	9.5

Sps. However, we could not receive any signal, and the system could not run with an extremely low I/Q sample rate or f_{BB} . We then increased the f_{BB} and I/Q sample rates, as shown in Table.II. We can clearly find a signal SNR jump when the I/Q sample rate increases to 100 kilo-sample-per-second (kSps) from 8 kSps. This is because when the I/Q sample rate is very low, sampling jitters distort the receiving signal and increase the noise floor of our target band.

IV. TREE SWALLOW VITAL-SIGNS MONITORING

Vital signs for animals with different body surface coverings are difficult to measure non-invasively. Substantial preparation procedures are often required for many veterinarian vital-sign sensing procedures. Electrocardiogram (ECG) and ultrasound need direct contact with the skin with a good electrical

or acoustic impedance match for heartbeat monitoring. The surface preparation may include shaving hair, fur, scales, or feathers of the sensing area. For respiratory monitoring, a thermistor or an airflow detector can be placed on the endotracheal tube [24] or face covering [25]. Anesthesia is often required and can cause a serious bias to the metabolic parameters. Furthermore, even without anesthesia, discomfort and distress are also serious concerns in addition to animal cruelty.

There is no previous research on using a non-invasive sensor that can directly retrieve the cardiopulmonary recording of the conscious resting small birds and no sufficient published records of adult or nestling tree swallow heart rate and respiratory rate. And the avian respiratory rate strongly correlates with its weight [26], [27]. Thus, we used two species, barn swallow and bank swallow, whose size and weight are similar to tree swallow, for reference. Their respiratory rates are 80 breath-per-minute (BPM) and 122 BPM, respectively [28].

We built a test platform based on the stirrer model to collect and benchmark tree swallow's respiratory and heartbeat signals. Parallel antenna and in-line antenna placement were mounted onto a 3D-printed fixture and connected with the USRP, as shown in Fig. 5(a). The I/Q sample rate and f_{BB} were set to 10^6 Sps and 10 kHz, respectively. Two 2-minute experiments with different antenna pairs were performed on a 14-day nestling and an adult tree swallow, respectively, as shown in Figs. 5(b) and (c). The magnitude derived from the regularized complex sensing signals was passed to a 5th-order low-pass Butterworth filter with a cutoff of 20 Hz and then down-sampled to 50 Sps. Two 5th-order band-pass Butterworth filters with cutoff frequencies of 0.5 and 5 Hz and

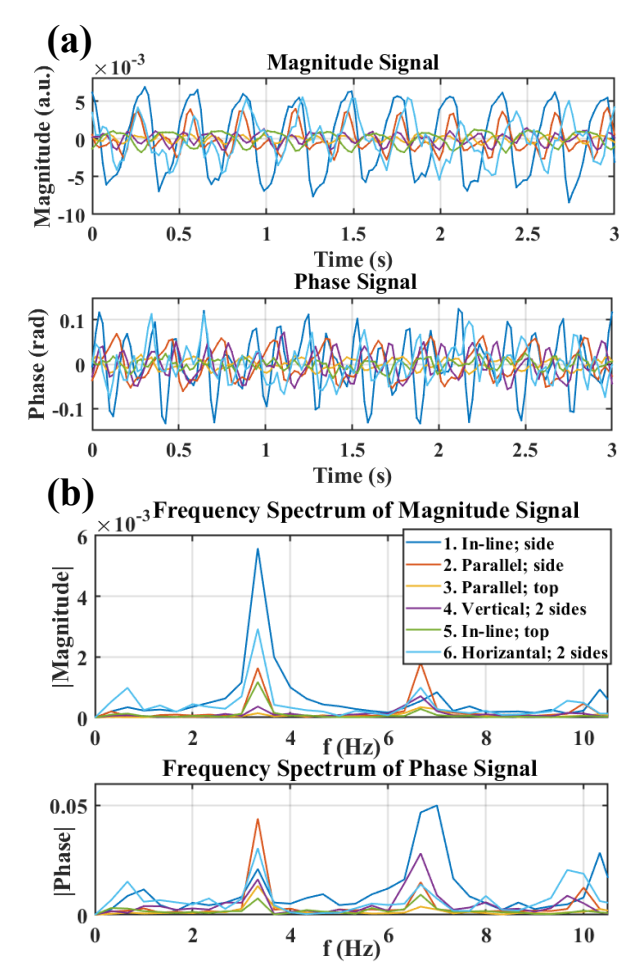


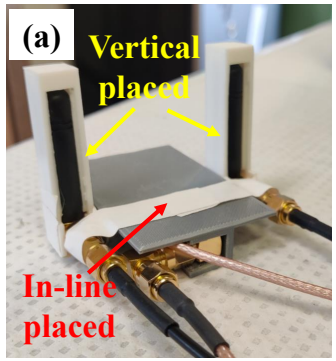
Fig. 4. Antenna placement comparison. (a) Time-domain signal; (b) Frequency spectrum.

cutoff frequencies of 5 and 16 Hz were used to subtract the respiratory and heartbeat signals, as shown in Figs. 6 (a), (b), and (c). From fast-Fourier transform (FFT), we can derive a 1.5 Hz respiration rate from different antenna placements for the adult bird and 2.8 Hz for the nestling bird, as shown in Fi. 6(d). Furthermore, we can also find a 6.8 Hz heart rate for the adult bird. Both respiratory and heart rates are close to the previous reports [26], [27].

V. Nestling Bird Respiration Monitoring

A. RF Sensor Design

For the metabolic monitoring of nestling birds within an air-tight box, we built an RF near-field sensor manufactured on a 4-layer printed circuit board (PCB) to accomplish a fully portable design for bird respiratory function monitoring. The air-tight requirement is to measure O2/CO2 variations accurately. Although cable fitting is possible, an all-in-one sensor design is more desirable for easy system configuration. The block diagram of the near-field RF sensing system, as shown in Fig. 7 (b), includes two main modules and two digital sensor peripherals. Two CC1310 SimpleLink sub-1 GHz ultra-low-power wireless microcontrollers are used as the sensing Tx and Rx. The transceivers employed quadrature I/Q modulation, where two channels of 12-bit I and O samples





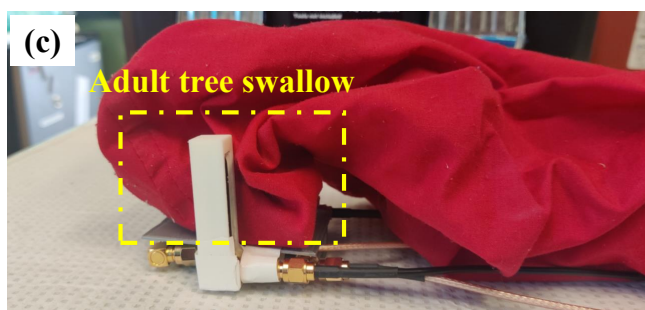


Fig. 5. (a) The tree swallow vital-sign sensing platform with one antenna pair vertically placed on the two sides and another pair in-line placed underneath; (b) The nestling tree swallow is sitting on the sensor; (c) The adult tree swallow sitting inside a red cloth bag.

were sampled at 2 kHz and accumulated into one 400-bytes cyclic buffer at the sensor Rx. Once the I/Q buffer was filled, the Rx radio core would bundle the I and Q samples with the temperature, accelerometer, and gyroscope readings to a micro SD card through a module of the serial peripheral bus (SPI). The temperature sensor (Texas Instrument TMP112) and inertial measurement unit (Bosch Sensortec BMI160) are connected by the inter-integrated-circuits (I2C) serial protocol. Our sensor is manufactured on a 4-layer printed circuit board (PCB), including two signal layers, one ground layer, and one power layer, as shown in Fig. 7 (a).

B. Experimental Setup and Protocol

A 40-minute experiment on a 13-days old nestling tree swallow was conducted. Following the previous design principles for high sensitivity, two antenna holder structures and placements were used to collect the bird's respiratory signal. As shown in Fig. 8(a), one sensor, labeled as 'sensor 1', was connected to a parallel placed PCB antenna (Taoglas pc.81) pair on top of 'sensor 2' and underneath the bird. The other sensor, labeled as 'sensor 2', was connected to the antenna pair vertically on the two sides, which were 5 cm separated. Frequency division multiple access (FDMA) was used to provide isolation between the channels of two sensors. Sensors 1 and 2 operated at 898 MHz and 868 MHz, respectively. The total surface size of the two sensors is 120 mm \times 70 mm. During the experiment, the nestling tree swallow was placed in an air-tight hard plastic box with a dimension of 190 mm \times 120 mm \times 80 mm. The glass box has constant air feeding and is placed inside a thermal controllable chamber, as shown in Fig. 8(b).

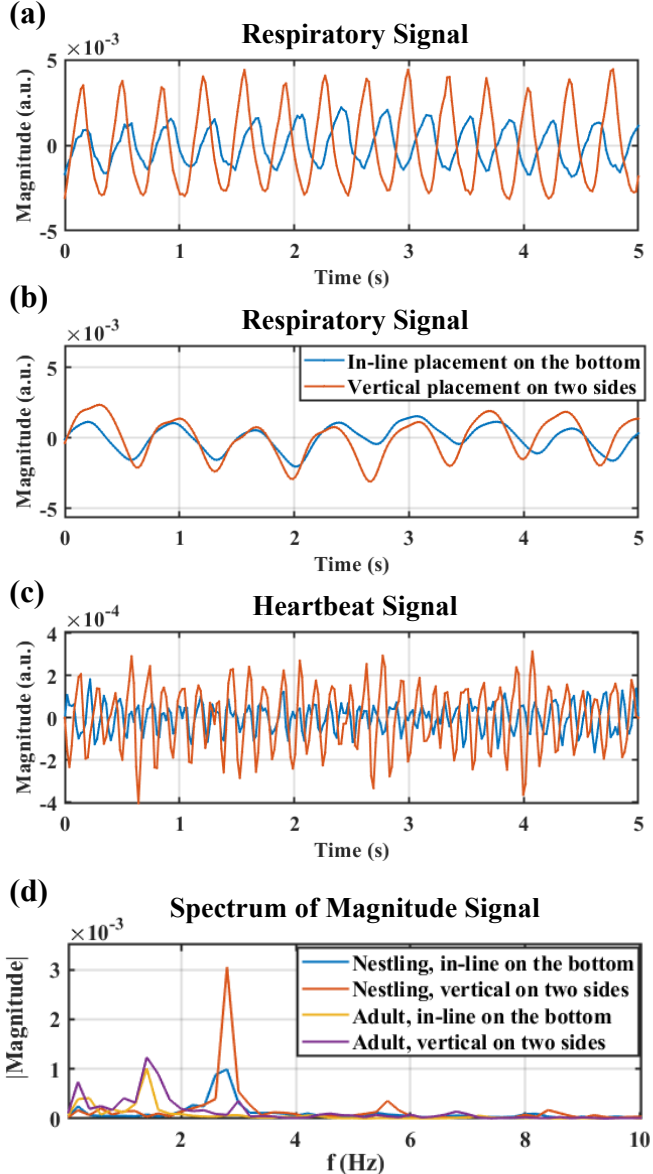


Fig. 6. 5s time-domain respiratory signals between the in-line placed and vertically placed antenna pair for adult and nestling tree swallows, as well as the heartbeat signals of the adult bird. (a) Nestling tree swallow respiratory signals; (b) Adult tree swallow respiratory signals; (c) Adult tree swallow heartbeat signals; (d) Frequency spectrum comparison for adult and nestling magnitude signals.

C. Experiment Result

Similar to the stirrer model setup, the sensor magnitude signal is first processed by a 5th-order band-pass Butterworth filter with a cutoff of $0.2 \, \text{Hz}$ and $10 \, \text{Hz}$ and then downsampled to $50 \, \text{samples}$ per second (SPS) in the pre-processing stage, as shown in Fig. 9 (a). The magnitude signal is then segmented into several 30-second epochs, in which a fast-Fourier transform (FFT) is performed to calculate the bird's respiratory frequency by the maximum peaks between $1.5 \, \text{Hz}$ to $3 \, \text{Hz}$ and $3 \, \text{Hz}$ to $6 \, \text{Hz}$. As shown in Fig. 9 (b), the signal from sensor 1 underneath the bird has a stronger 2^{nd} harmonic and lower signal power than that from sensor 2, which was connected to the two sides of the bird. Meanwhile, since the bird's body motion can distort the signal, as shown in Figs. 9 (b) and



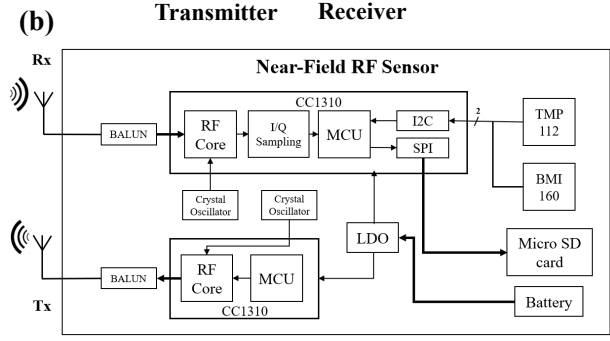


Fig. 7. (a) and (b) are the photos of the low-power near-field RF sensor PCB and its block diagram.

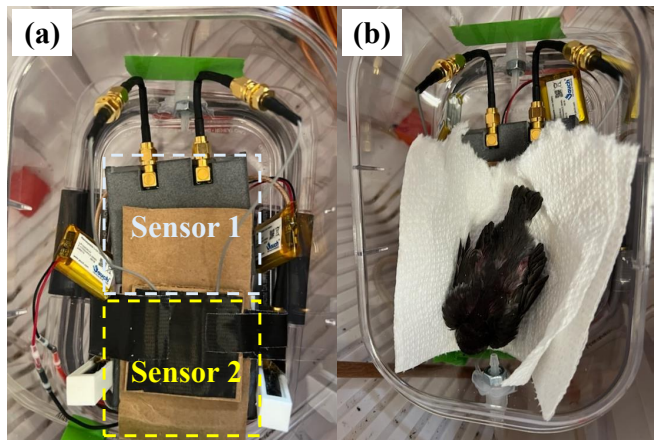


Fig. 8. (a) Photo of a two-sensor setup with vertically placed antennas on two sides and in-line placed on the bottom; (b) Photo of nestling tree swallow sitting on the sensor.

(c) during 32 minutes to 35 minutes, the noisy epochs were removed due to low power levels of the respiratory signals to the average power between 1 Hz to 10 Hz. The final respiratory rate and corresponding temperature are presented in Fig. 9 (d). The respiratory rates from the two sensors are very close, decreasing as time increases. We think this is because the handling disturbance from placing the bird in the chamber results in an elevated initial respiration rate. And as time goes by, the bird relaxes, which causes a respiratory rate decrease.

VI. CONCLUSION

In this paper, a RF sensor based on near-field sensing is presented to monitor minute motion hidden inside a structure or a conscious small animal. We explored the optimal antenna

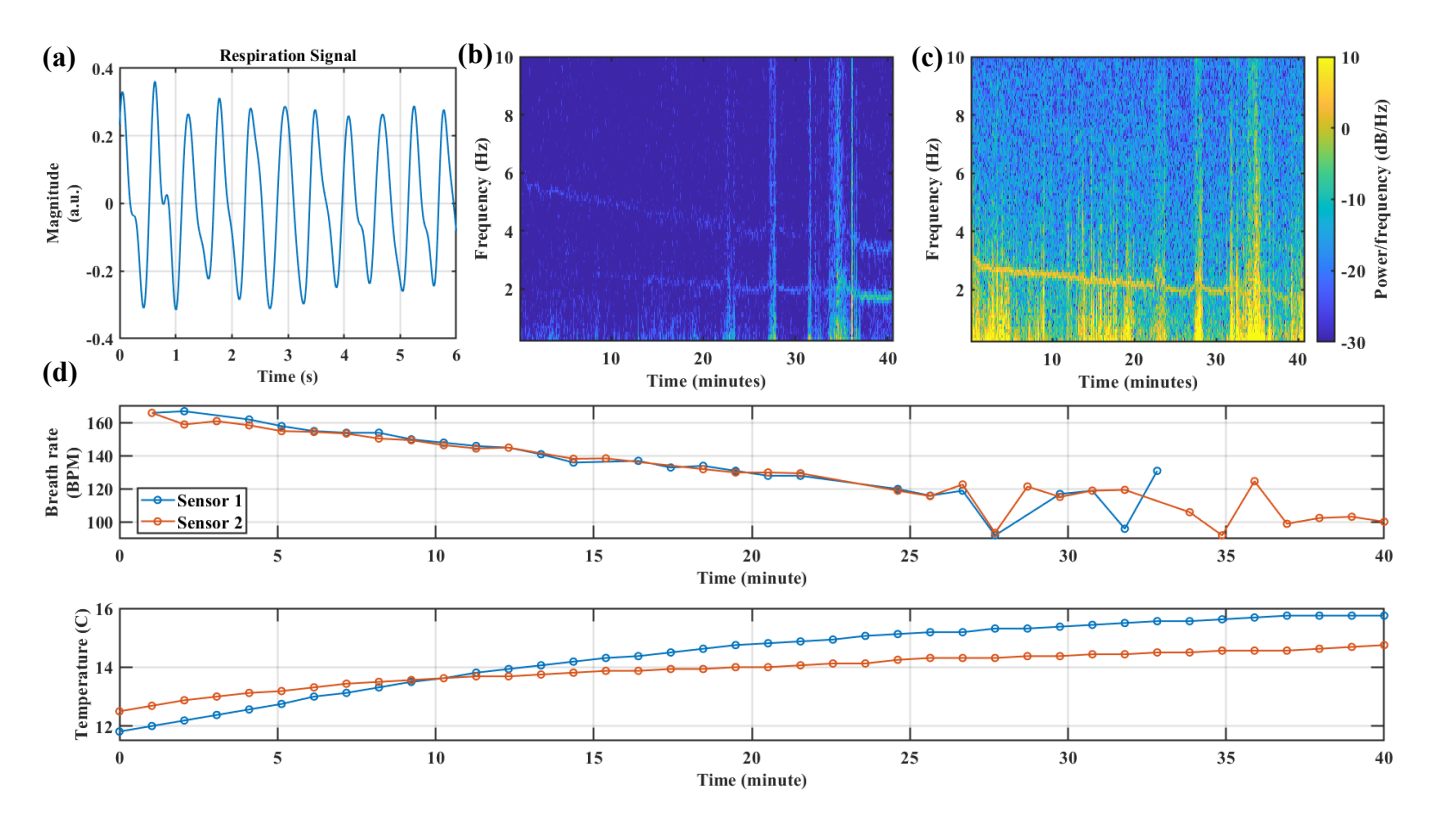


Fig. 9. (a) shows a 6 seconds recording of respiratory signal collected by sensor 1. (b) and (c) show the 40 min recordings' time-frequency spectrograms of sensor 1 and sensor 2, respectively. (d) presents the respiratory rate and temperature readings from the two sensors.

TABLE III
SUMMARY OF THE NEAR-FIELD RF SENSOR SYSTEM
CHARACTERISTICS

Parameters	Value	
PCB size	50 × 60 mm	
Weight (PCB)	22 g	
Weight (PCB and Package)	40 g	
Supply voltage	3.7 V	
Average current consumption	41 mA	
RF sensor carrier frequency (tunable)	868 MHz	
RF sensor transmitting power	0 dBm	
RF sensor sampling rate	2000 Sps	
Motion sensor sampling rate	20 Sps	

placement and sensor radio configuration experimentally by a stirrer model. An optimized setup of two PCB near-field RF sensors was then applied to a continuous recording of the respiration and motion of nestling tree swallow under ambient temperature variation. After design optimization of antenna placement and appropriate selection of transceiver parameters and signal processing methods, we demonstrated that near-field sensing can have high sensitivity for minuscule motion hidden inside structures or living body.

REFERENCES

- [1] C. M. Williams, A. Szejner-Sigal, T. J. Morgan, A. S. Edison, D. B. Allison, and D. A. Hahn, "Adaptation to low temperature exposure increases metabolic rates independently of growth rates," *Integrative and comparative biology*, vol. 56, no. 1, pp. 62–72, 2016.
- [2] W. Zuo, M. E. Moses, G. B. West, C. Hou, and J. H. Brown, "A general model for effects of temperature on ectotherm ontogenetic growth and development," *Proc. Royal Society B: Biological Sciences*, vol. 279, no. 1734, pp. 1840–1846, 2012.
- [3] A. Wojtowicz, A. Ubysz, and J. Michałek, "How vibrations affect steel-to-concrete adherence," in MATEC Web of Conferences, vol. 251. EDP Sciences, 2018, p. 02045.
- [4] A. Sabato, C. Niezrecki, and G. Fortino, "Wireless mems-based accelerometer sensor boards for structural vibration monitoring: a review," *IEEE Sensors Journal*, vol. 17, no. 2, pp. 226–235, 2016.
- [5] E. Song, Z. Xie, W. Bai, H. Luan, B. Ji, X. Ning, Y. Xia, J. M. Baek, Y. Lee, R. Avila *et al.*, "Miniaturized electromechanical devices for the characterization of the biomechanics of deep tissue," *Nature Biomedical Engineering*, vol. 5, no. 7, pp. 759–771, 2021.
- [6] M. Zanartu, J. C. Ho, S. S. Kraman, H. Pasterkamp, J. E. Huber, and G. R. Wodicka, "Air-borne and tissue-borne sensitivities of bioacoustic sensors used on the skin surface," *IEEE Transactions on Biomedical Engineering*, vol. 56, no. 2, pp. 443–451, 2009.
- [7] J. C. Lin, "Noninvasive microwave measurement of respiration," *Proc. IEEE*, vol. 63, no. 10, pp. 1530–1530, Oct 1975.
- [8] X. Ma, Y. Wang, X. You, J. Lin, and L. Li, "Respiratory pattern recognition of an adult bullfrog using a 100-ghz cw doppler radar transceiver," in 2019 IEEE MTT-S International Microwave Biomedical Conference (IMBioC), Nanjing, China, vol. 1, May 2019, pp. 1–3.
- [9] B. Schleicher, I. Nasr, A. Trasser, and H. Schumacher, "Ir-uwb radar demonstrator for ultra-fine movement detection and vital-sign monitoring," *IEEE Transactions on Microwave Theory and Techniques*, vol. 61, no. 5, pp. 2076–2085, 2013.
- [10] L. Ren, H. Wang, K. Naishadham, Q. Liu, and A. E. Fathy, "Non-invasive detection of cardiac and respiratory rates from stepped frequency continuous wave radar measurements using the state space method," in 2015 IEEE MTT-S International Microwave Symposium, Phoenix, AZ, USA. IEEE, 2015, pp. 1–4.

- [11] A. Mishra, W. McDonnell, J. Wang, D. Rodriguez, and C. Li, "Intermodulation-based nonlinear smart health sensing of human vital signs and location," *IEEE Access*, vol. 7, pp. 158 284–158 295, 2019.
- [12] D. Tang, V. G. R. Varela, D. V. Q. Rodrigues, D. Rodriguez, and C. Li, "A wi-fi frequency band passive biomedical doppler radar sensor," *IEEE Transactions on Microwave Theory and Techniques*, pp. 1–9, 2022.
- [13] D. Tang, D. V. Q. Rodrigues, M. C. Brown, and C. Li, "Dual null detection points removal and time-domain sensitivity analysis of a self-injection-locked radar for small-amplitude motion sensing," *IEEE Transactions on Microwave Theory and Techniques*, vol. 70, no. 9, pp. 4263–4272, 2022.
- [14] X. Hui and E. C. Kan, "Monitoring vital signs over multiplexed radio by near-field coherent sensing," *Nature Electronics*, vol. 1, no. 1, pp. 74–78, 2018.
- [15] X. Hui, T. B. Conroy, and E. C. Kan, "Near-field coherent sensing of vibration with harmonic analysis and balance signal injection," *IEEE Transactions on Microwave Theory and Techniques*, vol. 69, no. 3, pp. 1906–1916, 2021.
- [16] E. Pittella, S. Pisa, and M. Cavagnaro, "Breath activity monitoring with wearable uwb radars: Measurement and analysis of the pulses reflected by the human body," *IEEE Transactions on Biomedical Engineering*, vol. 63, no. 7, pp. 1447–1454, 2015.
- [17] J.-M. Muñoz-Ferreras, J. Wang, Z. Peng, R. Gómez-García, and C. Li, "From doppler to fmew radars for non-contact vital-sign monitoring," in 2018 2nd URSI Atlantic Radio Science Meeting (AT-RASC). IEEE, 2018, pp. 1–4.
- [18] F. Adib, H. Mao, Z. Kabelac, D. Katabi, and R. C. Miller, "Smart homes that monitor breathing and heart rate," in *Proc. 33rd Annual ACM Conference on Human Factors in Computing Systems, Seoul, Republic of Korea*, 2015, pp. 837–846.
- [19] X. Hui and E. C. Kan, "No-touch measurements of vital signs in small conscious animals," *Science Advances*, vol. 5, no. 2, p. eaau0169, 2019.
- [20] J. Zhou, P. Sharma, X. Hui, and E. C. Kan, "A wireless wearable rf sensor for brumation study of chelonians," *IEEE Journal of Electro*magnetics, RF and Microwaves in Medicine and Biology, vol. 5, no. 1, pp. 17–24, 2020.
- [21] X. Hui, J. Zhou, and E. C. Kan, "High-volume parallel mouse vitalsign monitoring with near-field coherent sensing," *IEEE Antennas and Wireless Propagation Letters*, vol. 19, no. 7, pp. 1152–1156, 2020.
- [22] R. E. Fields, "Evaluating compliance with fcc guidelines for human exposure to radiofrequency electromagnetic fields," *OET Bulletin*, vol. 65, no. 10, 1997.
- [23] J. Zhou, T. B. Conroy, G. Xu, and E. C. Kan, "Morphology transformation and content selection of near-field rf sensing by complex vector injection," *IEEE Journal of Electromagnetics, RF and Microwaves in Medicine and Biology*, pp. 1–11, 2022.
- [24] B. P. Monitoring, "Monitoring vital signs in clinical and research animals," *Current Separations*, vol. 16, no. 2, p. 44, 1997.
- [25] A. Smith, G. Bond, and J. Nordstrom, "Measurement of heart and respiratory frequencies in chickens," *Poultry Science*, vol. 45, no. 4, pp. 704–708, 1966.
- [26] W. A. Calder, "Respiratory and heart rates of birds at rest," *The Condor*, vol. 70, no. 4, pp. 358–365, 1968.
- [27] R. C. Lasiewski and W. A. Calder Jr, "A preliminary allometric analysis of respiratory variables in resting birds," *Respiration physiology*, vol. 11, no. 2, pp. 152–166, 1971.
- [28] P. B. Frappell, D. Hinds, and D. Boggs, "Scaling of respiratory variables and the breathing pattern in birds: an allometric and phylogenetic approach," *Physiological and Biochemical Zoology*, vol. 74, no. 1, pp. 75–89, 2001.



Jianlin Zhou received the B.S. degree in electronics and information engineering from Nanjing University of Science and Technology, Nanjing, China in 2013, and the M.S. degree in electrical and computer engineering from Northeastern University, Boston, MA in 2016. He is currently pursuing the Ph.D. degree in electrical and computer engineering at Cornell University, Ithaca, NY, USA.

He has previously worked as a research support associate on ingestible electronics design

for drug delivery and bio-sensing in Robert Langer Lab at Massachusetts Institute of Technology from 2016 to 2018. His research interests include radio frequency, vital signs monitoring, wearable sensor design, and electromagnetic sensing system optimization.



Conor C. Taff received a B.A. degree in Environmental Science from Skidmore College in 2005 and a Ph.D. in Animal Behavior from the University of California—Davis in 2013. At UC Davis, he also completed a postdoctoral fellowship from the USDA National Institute of Food and Agriculture studying the role of wild birds in foodborne disease transmission. In 2015 he joined the Cornell Lab of Ornithology and Department of Ecology & Evolutionary Biology as a postdoctoral fellow and he is currently a

Research Associate at Cornell. His research interests include stress physiology, behavioral ecology, and the breeding biology of wild bird populations.

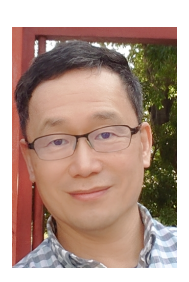


David Chang van Oordt received a BSc in biology from Universidad Peruana Cayetano Heredia, Lima, Peru in 2013. He then received an MSc in ecology and evolutionary biology from Cornell University, Ithaca, NY, USA in 2018. Currently, he is pursuing a PhD in ecology and evolutionary Biology at Cornell University, Ithaca, NY, USA. His research interests include ecophysiology, ecoimmunology, life history evolution and ornithology.



Maren N. Vitousek received a BA in biology from Amherst College in 2002, and then a PhD in ecology and evolutionary biology from Princeton University in 2008. After postdoctoral positions at the Max Planck Institute and the University of Colorado, Boulder, she joined the Department of Ecology and Evolutionary Biology at Cornell as an assistant professor in 2016, and was promoted to associate professor in 2020. Her research interests include evolutionary physiology and animal behavior, with a particular interest in

how animals cope with stress.



Edwin C. Kan received the B.S. degree from National Taiwan University in 1984, and the M.S. and Ph.D. degrees from University of Illinois, Urbana-Champaign in 1988 and 1992, respectively, all in electrical engineering. He has served in the Air Force, Taiwan, R. O. China as a second lieutenant from 1984 to 1986. In January 1992, he joined Dawn Technologies as a Principal CAD Engineer. He was then with Stanford University as a Research Associate from 1994 to 1997. In 1997, he joined the School of Electrical and

Computer Engineering, Cornell University, Ithaca, NY as an assistant professor, where he is now a professor. His research interests include RF biosensors, RFID, RF sensors for smart buildings, CMOS technology, Flash memory, molecular sensors, and technology computer-aided design (TCAD).